

March 2022

# Incident Velocity–Recoil Angle Distribution and Angular Recoil–Energy Spectrum of 3-Dimensional WIMP–Nucleus Scattering Events

CHUNG-LIN SHAN

*Preparatory Office of the Supporting Center for Taiwan Independent Researchers  
P.O.BOX 21 National Yang Ming Chiao Tung University, Hsinchu City 30099, Taiwan, R.O.C.*

*E-mail: clshan@tir.tw*

## Abstract

In this paper, as a supplementary of our study on the angular distribution of the recoil flux of WIMP–scattered target nuclei and on that of the WIMP effective scattering velocity distribution, we investigate the scattering probability distribution of the WIMP incident velocity versus the nuclear recoil angle in narrow recoil energy windows for different WIMP masses and target nuclei. Our simulation results show that, not only the velocity distribution of incident halo WIMPs, but also a factor of the recoil angle could affect the scattering probability distribution of the available incident velocity–recoil angle combination in a given recoil energy window. Consequently, the 1-D WIMP “effective” velocity distribution corresponding to the considered narrow energy window would not be consistent with that cut simply from the (generating) velocity distribution of incident halo WIMPs. And its contribution to the differential WIMP–nucleus scattering event rate in the considered energy window could thus not be simply estimated by integrating over the 1-D theoretical velocity distribution (of entire halo WIMPs).

arXiv:2203.05805v1 [hep-ph] 11 Mar 2022

# 1 Introduction

Direct Dark Matter (DM) detection experiments aiming to observe scattering signals of Weakly Interacting Massive Particles (WIMPs) off target nuclei would still be the most reliable experimental strategy for identifying Galactic DM particles and determining their properties [1, 2, 3, 4]. While most direct DM detection experiments measure only recoil energies deposited in underground detectors, the “directional” direct detection experiments could provide additional 3-dimensional information (recoil tracks and/or head–tail senses) of (elastic) WIMP–nucleus scattering events as a promising experimental strategy for discriminating WIMP signals from isotropic backgrounds and/or some incoming–direction–known astronomical events [5, 6, 7].

As the preparation for our future study on the development of data analysis procedures for using and/or combining 3-D information offered by directional Dark Matter detection experiments, we have developed the double Monte Carlo scattering–by–scattering simulation package for the 3-D elastic WIMP–nucleus scattering process [8] and studied the angular distributions of the recoil flux and energy of WIMP–scattered target nuclei in different celestial coordinate systems [9, 10]. We have also introduced and demonstrated the target and WIMP–mass dependent “effective” velocity distribution of halo WIMPs (not only impinging on but also) scattering off target nuclei (in different celestial coordinate systems) [11], which could be pretty different from the velocity distribution of incident Galactic WIMPs [12, 13].

During these works, the dependence of the recoil energy on the recoil angle and the incoming velocity of the scattering WIMPs as well as the dependence of the differential scattering cross section on the recoil angle and the nuclear form factor(s) have been noticed and discussed in detail in Ref. [14]. It has been found that, firstly, for a given WIMP incident velocity, different recoil angles corresponding to different recoil energies should have different scattering probabilities and would contribute to the differential event rate differently [14]. Secondly, for a given recoil energy (window), different available incident velocity–recoil angle combinations should have different scattering probabilities and would contribute to the differential event rate differently [14]. These observations indicate further possible incompleteness of the conventionally used expressions for the (double) differential WIMP–nucleus scattering event rates in (directional) direct DM detection physics [14] as well as predict totally different 3-D distribution patterns of the WIMP–induced nuclear recoil flux (and energy) from those provided in several earlier works (see e.g. Refs. [15, 16, 6, 17, 7]). Hence, in this paper, we investigate the scattering distribution of the WIMP incident velocity versus the nuclear recoil angle in narrow recoil energy windows for different target nuclei and WIMP masses, in order to provide more detailed information on its contribution to the (double) differential scattering event rates.

The remainder of this paper is organized as follows. In Sec. 2, we review briefly some basic considerations to factors, which could affect the scattering probability of an incident velocity–recoil angle combination. Then the scattering distributions on the incident velocity vs. recoil angle plane as well as the angular distributions of the recoil fluxes for a light and a heavy WIMP masses scattering off the light  $^{19}\text{F}$  and the heavy  $^{129}\text{Xe}$  nuclei will be presented and discussed in Secs. 3 and 4, respectively. We summarize our observations in Sec. 5.

## 2 Basics

This work is based on our double Monte Carlo scattering–by–scattering simulations for 3-D elastic WIMP–nucleus scattering described in detail in Refs. [8, 9]. In this section, we review only briefly some basic considerations to factors, which could affect the scattering probability of an incident velocity–recoil angle combination.

Consider microscopically one incident halo WIMP of a mass  $m_\chi$  moving with an incoming velocity  $\mathbf{v}_{\chi,\text{Lab}}$  and scattering off a target nucleus of a mass  $m_N$ . The kinetic energy of the incident (and scattering) WIMP in the laboratory (detector at rest) coordinate system can be given by

$$E_\chi = \frac{1}{2}m_\chi|\mathbf{v}_{\chi,\text{Lab}}|^2 = \frac{1}{2}m_\chi v_{\chi,\text{Lab}}^2. \quad (1)$$

Then the recoil energy of the scattered target nucleus (in the laboratory coordinate system) can be expressed as a function of the recoil angle  $\eta$ , or, equivalently, the “equivalent” recoil angle  $\theta_{N_R,\chi_{\text{in}}}$  by [8]

$$\begin{aligned} Q &= \left[ \frac{4m_\chi m_N}{(m_\chi + m_N)^2} \cos^2(\eta) \right] E_\chi = \left[ \left( \frac{2m_{r,N}^2}{m_N} \right) v_{\chi,\text{Lab}}^2 \right] \cos^2(\eta) \\ &= \left[ \left( \frac{2m_{r,N}^2}{m_N} \right) v_{\chi,\text{Lab}}^2 \right] \sin^2(\theta_{N_R,\chi_{\text{in}}}). \end{aligned} \quad (2)$$

Here  $m_{r,N} \equiv m_\chi m_N / (m_\chi + m_N)$  is the WIMP–nucleus reduced mass,  $\eta$  is the recoil angle of the scattered nucleus (the angle between the recoil direction and the WIMP incoming velocity) [8], and  $\theta_{N_R,\chi_{\text{in}}} = \pi/2 - \eta$  (i.e. the complementary angle of  $\eta$ ) is the elevation of the nuclear recoil direction in the incoming–WIMP coordinate system [8].

Conventionally, people only use Eq. (2) with the minimal (maximal equivalent) recoil angle of  $\eta = 0$  ( $\theta_{N_R,\chi_{\text{in}}} = 90^\circ$ ) to define the minimal–required incoming velocity of incident WIMPs, which can transfer the considered recoil energy  $Q^*$  to a target nucleus:

$$v_{\text{min}}^* = v_{\text{min}}(Q^*) = \sqrt{\frac{m_N}{2m_{r,N}^2}} \sqrt{Q^*} = \alpha \sqrt{Q^*}, \quad (3)$$

where  $\alpha \equiv \sqrt{m_N/2m_{r,N}^2}$  is the transformation constant. However, as discussed in detail in Ref. [14], the expression (2) indicates that the WIMP–induced nuclear recoil energy should be considered as a two–variable function of the WIMP incident velocity  $v_{\chi,\text{Lab}}$  and the recoil angle  $\eta$ , as shown in Fig. 1. For incident WIMPs with (monotonically) the given incoming velocity  $v_{\text{min}}^*$ ,  $Q^*$  can be considered as the “maximal transferable” recoil energy. This implies, firstly, that, due to the nuclear form factor suppression, the probability of WIMP scattering events with a small or even zero (large equivalent) recoil angle and thus a large recoil energy around  $Q^*$  should be strongly reduced [14].

Secondly, along the (blue) equal–recoil–energy– $Q^*$  contour, one has

$$\eta(Q^*, v_{\chi,\text{Lab}}) = \cos^{-1} \left( \frac{\alpha \sqrt{Q^*}}{v_{\chi,\text{Lab}}} \right), \quad (4a)$$

or, equivalently,

$$\theta_{N_R,\chi_{\text{in}}}(Q^*, v_{\chi,\text{Lab}}) = \sin^{-1} \left( \frac{\alpha \sqrt{Q^*}}{v_{\chi,\text{Lab}}} \right). \quad (4b)$$

Although the strength of the nuclear form factor suppression (depending only on the recoil energy  $Q^*$ ) is equal, the velocity distribution of incident halo WIMPs affects the scattering probabilities

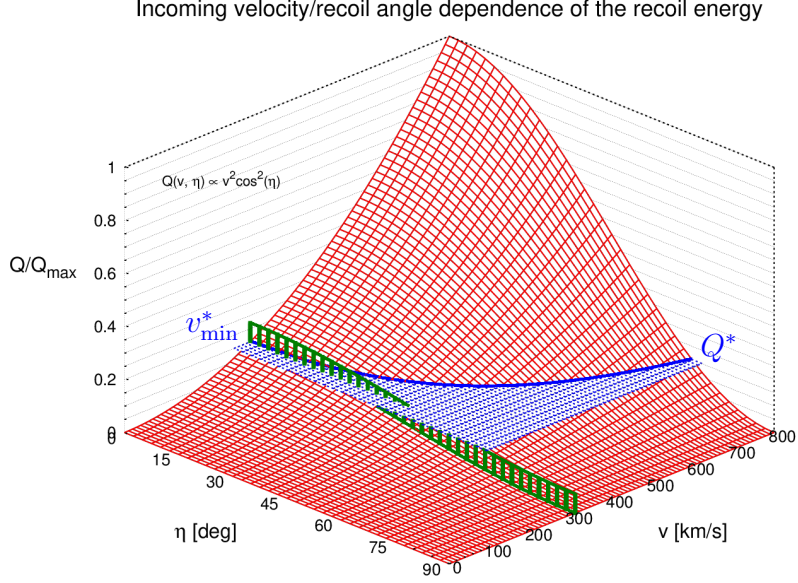


Figure 1: The 2-D dependence of the recoil energy on the incoming velocity of incident WIMPs  $v_{\chi, \text{Lab}}$  and the recoil angle  $\eta$  given in Eq. (2). The green vertical fence indicates the given WIMP incident velocity  $v_{\text{min}}^*$ , while the blue plane is the equal-recoil-energy plane of the corresponding energy  $Q^*$ .

of different  $v_{\chi, \text{Lab}}-\eta$  combinations<sup>1</sup>.

Thirdly and most importantly, from the conventionally used expression for the differential WIMP–nucleus scattering cross section as the function of the absolute value of the momentum transfer from the incident WIMP to the scattered nucleus [1, 2, 3]:

$$d\sigma = \frac{1}{v_{\chi, \text{Lab}}^2} \left( \frac{1}{4m_{\text{r}, \text{N}}^2} \right) \left[ \sigma_0^{\text{SI}} F_{\text{SI}}^2(q) + \sigma_0^{\text{SD}} F_{\text{SD}}^2(q) \right] dq^2, \quad (6)$$

with  $q = \sqrt{2m_{\text{N}}Q}$ , the spin-independent/dependent (SI/SD) total cross sections ignoring the nuclear form factor suppressions,  $\sigma_0^{(\text{SI}, \text{SD})}$ , as well as the elastic nuclear form factors corresponding to the SI/SD WIMP interactions,  $F_{(\text{SI}, \text{SD})}(q)$ , the differential cross section  $d\sigma$  with respect to the differential (equivalent) recoil angles  $d\eta$  ( $d\theta_{\text{NR}, \chi_{\text{in}}}$ ) have been derived as [8, 14]

$$\left| \frac{d\sigma}{d\eta} \right| = \left[ \sigma_0^{\text{SI}} F_{\text{SI}}^2(Q) + \sigma_0^{\text{SD}} F_{\text{SD}}^2(Q) \right] \sin(2\eta), \quad (7a)$$

<sup>1</sup>Note that, from Eqs. (4a) and (4b), one can find “maximal (minimal) available” (equivalent) recoil angles for transferring the considered recoil energy  $Q^*$  as

$$\eta_{\text{max}}(Q^*) = \cos^{-1} \left( \frac{\alpha \sqrt{Q^*}}{v_{\chi, \text{cutoff}}} \right), \quad (5a)$$

and

$$\theta_{\text{NR}, \chi_{\text{in}}, \text{min}}(Q^*) = \sin^{-1} \left( \frac{\alpha \sqrt{Q^*}}{v_{\chi, \text{cutoff}}} \right), \quad (5b)$$

where  $v_{\chi, \text{cutoff}} \simeq 800$  km/s is a cut-off velocity of incident halo WIMPs (in the Equatorial/laboratory coordinate systems).

and

$$\frac{d\sigma}{d\theta_{N_R, \chi_{in}}} = \left[ \sigma_0^{\text{SI}} F_{\text{SI}}^2(Q) + \sigma_0^{\text{SD}} F_{\text{SD}}^2(Q) \right] \sin(2\theta_{N_R, \chi_{in}}), \quad (7b)$$

respectively. Note that we use here the absolute value of  $d\sigma/d\eta$ , since the recoil energy  $Q$  decreases while the recoil angle  $\eta$  increases. Remind also that the recoil energy  $Q$  here should be considered as the function of  $v_{\chi, \text{Lab}}$  and  $\eta$  ( $\theta_{N_R, \chi_{in}}$ ) given in Eq. (2).

Moreover, by taking into account the proportionality of the WIMP flux to the WIMP incident velocity, the scattering probability of incident halo WIMPs *moving with the given incoming velocity*  $v_{\chi, \text{Lab}}$  and scattering off target nuclei going into an (equivalent) recoil angle between  $\eta \pm d\eta/2$  ( $\theta_{N_R, \chi_{in}} \pm d\theta_{N_R, \chi_{in}}/2$ ) with a recoil energy of  $Q \pm dQ/2$  can generally be expressed by [8, 14]

$$f_{N_R}(v_{\chi, \text{Lab}}, \eta) = \frac{v_{\chi, \text{Lab}}}{v_{\chi, \text{cutoff}}} \left[ \sigma_0^{\text{SI}} F_{\text{SI}}^2(Q) + \sigma_0^{\text{SD}} F_{\text{SD}}^2(Q) \right] \sin(2\eta), \quad (8a)$$

and

$$f_{N_R}(v_{\chi, \text{Lab}}, \theta_{N_R, \chi_{in}}) = \frac{v_{\chi, \text{Lab}}}{v_{\chi, \text{cutoff}}} \left[ \sigma_0^{\text{SI}} F_{\text{SI}}^2(Q) + \sigma_0^{\text{SD}} F_{\text{SD}}^2(Q) \right] \sin(2\theta_{N_R, \chi_{in}}). \quad (8b)$$

These two expressions indicate clearly that, firstly, “head-on” (zero-recoil-angle,  $\eta = 0$ ) scattering events should be impossible. Secondly, the scattering probability distribution on the incident velocity versus the (equivalent) recoil angle ( $v_{\chi, \text{Lab}}-\eta$  ( $\theta_{N_R, \chi_{in}}$ )) plane would be (much) more complicated as people thought earlier. Remind that so far it could be understood that the scattering probability distribution depends at least on the velocity distribution of incident WIMPs, the nuclear form factor suppression of target nuclei, which depends further on their atomic mass and the WIMP mass, as well as the recoil-angle constraint on the differential scattering cross section.

### 3 Scattering by light 20-GeV WIMPs

As discussed in detail in Ref. [14] and reviewed briefly in Sec. 2, in different (narrow) recoil energy window, the scattering probability of each available WIMP incident velocity–nuclear recoil angle combination and its contribution to the differential WIMP–nucleus scattering event rate should be different. Hence, in this and the next sections, following our earlier work on the angular distribution of the WIMP–induced nuclear recoil flux [9]<sup>2</sup>, we reduce the simulated energy window to a width of only 5 keV and then investigate the scattering probability distribution on the WIMP incident velocity versus nuclear recoil angle plane.

In this section, we consider at first the case of a light WIMP mass of  $m_\chi = 20$  GeV. Two spin-sensitive nuclei used frequently in (directional) direct DM detection experiments: <sup>19</sup>F and <sup>129</sup>Xe have been considered as our targets<sup>3</sup>. As in our earlier works presented in Refs. [12, 13,

---

<sup>2</sup>Remind that we generate first a *3-dimensional velocity* of each incident WIMP in the Galactic coordinate system according to the theoretical isotropic Maxwellian velocity distribution and transform it to the laboratory coordinate system [8]. Then, in the laboratory (more precisely, the incoming–WIMP) coordinate system, we generate an *equivalent recoil angle* of a scattered target nucleus and validate this candidate scattering event according to the criterion (8b) [8]. Remind also that, in our double Monte Carlo simulation procedure, the induced recoil energy is determined by the WIMP incident velocity  $v_{\chi, \text{Lab}}$  and the equivalent recoil angle  $\theta_{N_R, \chi_{in}}$  through Eq. (2).

<sup>3</sup>Although Xe is (so far) not used in directional direct detection experiments, our simulation results shown in Secs. 3.2 and 4.2 would be similar to those with the <sup>127</sup>I nucleus.

9, 11, 10], the SI (scalar) WIMP–nucleon cross section in Eqs. (8a) and (8b) has been fixed as  $\sigma_{\chi\text{p}}^{\text{SI}} = 10^{-9}$  pb, while the effective SD (axial–vector) WIMP–proton/neutron couplings have been tuned as  $a_{\text{p}} = 0.01$  and  $a_{\text{n}} = 0.7a_{\text{p}} = 0.007$ , respectively. 5,000 experiments with 500 *accepted* events on average (Poisson–distributed) in one entire year in one experiment for one target nucleus have been simulated.

For readers’ reference, all simulation results demonstrated in this paper (and more) can be found “in animation” on our online (interactive) demonstration webpage [18].

### 3.1 20-GeV WIMPs off $^{19}\text{F}$ nuclei

We consider at first the case of light WIMPs of  $m_{\chi} = 20$  GeV scattering off light  $^{19}\text{F}$  target nuclei.

In Figs. 2(a) and 2(b), we show the scattering probability distributions of the available combinations of the incident WIMP velocity  $v_{\chi,\text{Lab}}$  versus the (equivalent) recoil angle  $\theta_{\text{Nr},\chi_{\text{in}}}$  (left axis) and also  $\eta$  (right axis) in the recoil energy windows between 0 and 100 (20) keV, respectively<sup>4</sup>. The horizontal color bar on the top of the plot indicates the mean value of the recorded event number (averaged over all simulated experiments) in each  $v_{\chi,\text{Lab}}-\theta_{\text{Nr},\chi_{\text{in}}}$  ( $\eta$ ) bin in unit of the average value of the *non-empty* bins (500 events / 192 (156) bins  $\cong$  2.60 (3.21) events/bin, respectively). The dashed golden curve in Fig. 2(b) indicates the equal–recoil–energy contour of  $\eta(Q = 20 \text{ keV}, v_{\chi,\text{Lab}})$  given in Eq. (4a) (i.e., the blue interaction curve in Fig. 1). As references, in the lower part of each plot, the dashed blue curve indicates the theoretically predicted shifted Maxwellian velocity distribution given in Eq. (7) of Ref. [11] for generating incident halo WIMPs, whereas the solid red histogram is the actual (effective) velocity distribution of the scattering WIMPs, which has been normalized to have the same height as the theoretical curve.

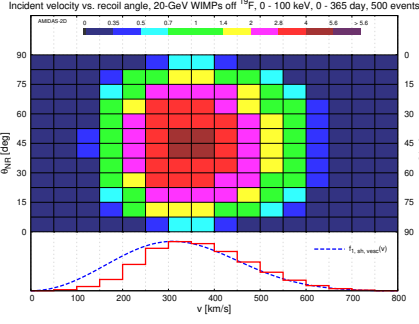
It can be found that, due to the factor of  $\sin(2\eta)$  in the expression (8a) for the scattering probability as well as the Gaussian–like WIMP velocity distribution, the most frequent incident velocity–recoil angle combinations would be around  $\eta \simeq 45^\circ$  and  $v_{\chi,\text{Lab}} \simeq 340$  km/s, which is a little bit larger than the average velocity of entire halo WIMPs of  $\bar{v}_{\text{Lab}} \simeq 331$  km/s, as can also be seen directly by comparing the (red) histograms with the (blue) theoretical curves.

Moreover, in Figs. 2(c) to 2(f), we slice the energy window up to 5 keV each<sup>5</sup>. Now the dependence of the scattering probability distributions on the available incident velocity–recoil angle combinations can be seen more clearly. Here, as a reference, the dashed red vertical line in each plot indicates the minimal–required WIMP incident velocity  $v_{\text{min}}$  estimated by Eq. (3) with the lower bound of the energy window. As expected, all available incident velocity–recoil angle combinations are in the area enclosed by the equal–recoil–energy contour(s). Constrained by the (most important)  $\sin(2\eta)$  factor, the scattering probabilities always reduce strongly (almost vanish) around zero recoil angle ( $\eta \simeq 0$ ), although the distributions of the recoil angle shift towards smaller  $\eta$  with the raising energy window. Additionally, the (red) WIMP “effective” velocity distributions corresponding to different energy windows seem also to be different from each other and those cut simply from the (blue) compared shifted Maxwellian velocity distribution by the minimal–required WIMP incident velocities (the dashed red vertical lines). This can be observed more clearly in Figs. 2(e) and 2(f) (as well as in Figs. 4(d) and 4(e)).

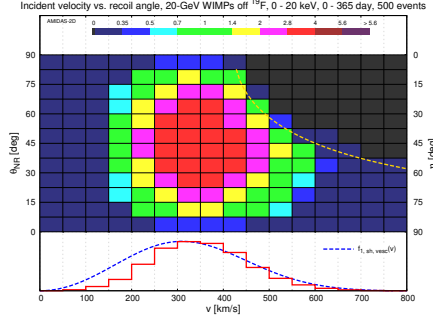
Correspondingly, Figs. 2(g) to 2(j) show the angular distributions of the WIMP–induced nuclear recoil flux (in unit of the all–sky average value) observed in the Equatorial coordinate system [12, 8]. The dark–green stars indicate the opposite direction of the Solar Galactic move-

<sup>4</sup>Interested readers can click each row of the plots in Figs. 2, 4, 5, and 6 to open the corresponding webpage of animated demonstrations (for more considered target nuclei/WIMP masses).

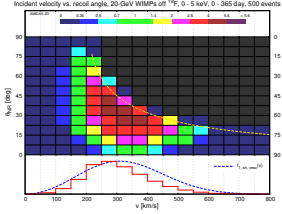
<sup>5</sup>Note that 500 accepted events on average in “each (5-keV)” energy window have been simulated.



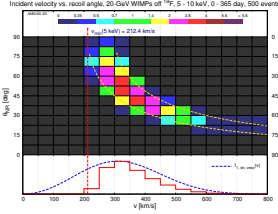
(a) 500 events in 0 – 100 keV



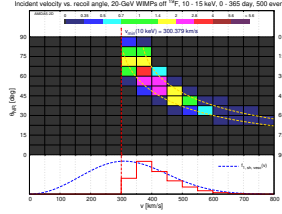
(b) 500 events in 0 – 20 keV



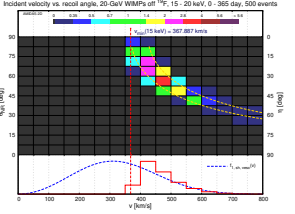
(c) 0 – 5 keV



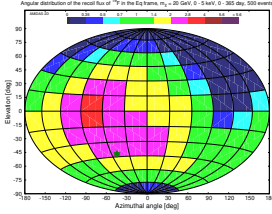
(d) 5 – 10 keV



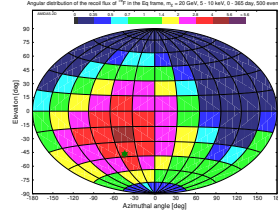
(e) 10 – 15 keV



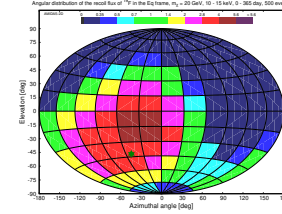
(f) 15 – 20 keV



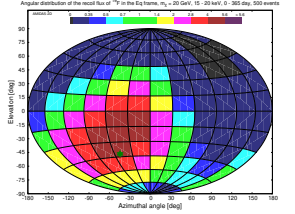
(g) 0 – 5 keV



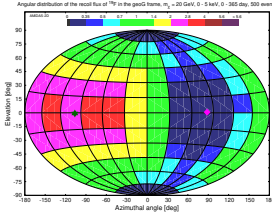
(h) 5 – 10 keV



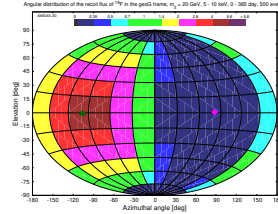
(i) 10 – 15 keV



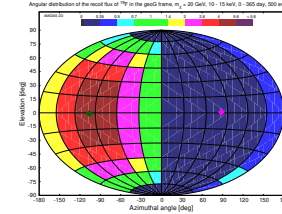
(j) 15 – 20 keV



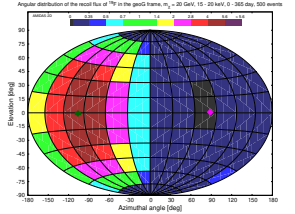
(k) 0 – 5 keV



(l) 5 – 10 keV



(m) 10 – 15 keV



(n) 15 – 20 keV

Figure 2: (a) – (f) The scattering probability distributions of the available  $v_{\chi, \text{Lab}} - \theta_{N_{R, \chi \text{in}}} (\eta)$  combinations for the case of 20-GeV WIMPs scattering off  $^{19}\text{F}$  in six different recoil energy windows. 500 accepted WIMP scattering events on average (Poisson-distributed) in one entire year in one experiment for one target nucleus have been simulated and binned into 16  $v_{\chi, \text{Lab}}$  bins  $\times$  12 angular  $\theta_{N_{R, \chi \text{in}}} (\eta)$  bins. While the dashed golden curve(s) in the upper part of each plot indicate(s) the equal-recoil-energy contour(s) of (the lower and) the upper bound(s) of the considered energy window, the dashed red vertical line indicates  $v_{\min}$  estimated by Eq. (3) with the lower bound of the energy window. The dashed blue curve in the lower part of each plot indicates the generating shifted Maxwellian velocity distribution of halo WIMPs given in Eq. (7) of Ref. [11], whereas the solid red histogram is the actual (effective) velocity distribution of the scattering WIMPs. Note that each histogram has been normalized to have the same height as the theoretical curve. (g) – (j) and (k) – (n) The corresponding angular distributions of the WIMP-induced nuclear recoil flux (in unit of the all-sky average value) observed in the Equatorial and the “geocentric” Galactic coordinate systems, respectively [12, 8]. The magenta diamonds (dark-green stars) indicate the (opposite) direction of the Solar Galactic movement [12, 8].

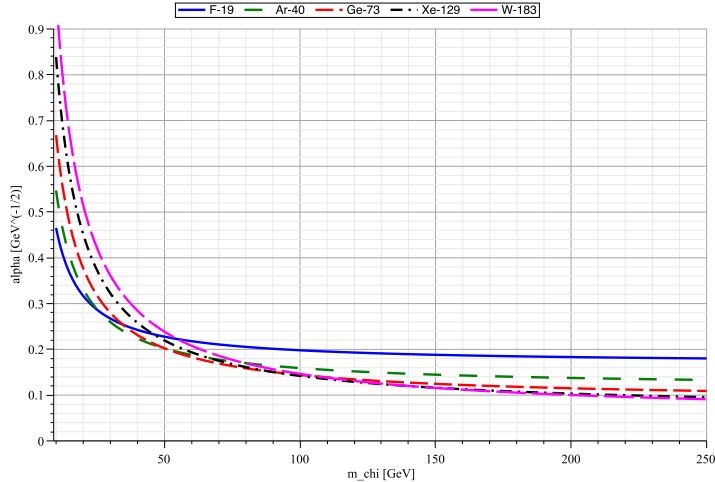


Figure 3: The WIMP–mass dependence of the transformation constant  $\alpha$  given in Eq. (3). Five frequently used target nuclei:  $^{19}\text{F}$  (solid blue),  $^{40}\text{Ar}$  (rare–dashed green),  $^{73}\text{Ge}$  (dashed red),  $^{129}\text{Xe}$  (dash–dotted black), and  $^{183}\text{W}$  (long–dashed magenta) have been considered.

ment [12, 8]:  $42.00^\circ\text{S}$ ,  $50.70^\circ\text{W}$ . The differences between the recoil–flux distribution patterns can be seen obviously. The higher the considered energy window, the smaller the (most) frequent recoil angle  $\eta$  and thus the more concentrated the nuclear recoil flux. It would however be interesting to notice that the maxima of the recoil flux in all four considered energy windows would *not* match the so–called “WIMP–wind” direction (the opposite direction of the Solar Galactic movement), but shift *northerly*.

Finally, for readers’ comparisons with the plots shown in e.g. Refs. [15, 16, 6, 7], in Figs. 2(k) to 2(n), we provide the corresponding angular recoil–flux distributions (in unit of the all–sky average value) observed in a “geocentric” Galactic coordinate system<sup>6</sup>. While the dark–green stars indicate the opposite direction of the Solar Galactic movement [12, 8]:  $0.60^\circ\text{S}$ ,  $98.78^\circ\text{W}$ , the magenta diamonds indicate additionally the moving direction of the Solar system:  $0.60^\circ\text{N}$ ,  $81.22^\circ\text{E}$ . Besides a clear north–south–sky symmetry, the recoil–flux distribution patterns on the east and west side of the sky divided by the opposite direction of the Solar Galactic movement (the green star) show asymmetric intensens and decreasing gradients: (the decrease of) the recoil fluxes on the inner (east) sky are clearly larger (and sharper) than those on the outer (west) sky.

### 3.2 20-GeV WIMPs off $^{129}\text{Xe}$ nuclei

In this subsection, we consider a heavy nucleus  $^{129}\text{Xe}$  as our detector target.

As shown in Fig. 3, for WIMP masses  $m_\chi \lesssim 45$  GeV, the transformation constant  $\alpha$  given in Eq. (3) for the  $^{19}\text{F}$  nucleus (solid blue) is smaller than that for the  $^{129}\text{Xe}$  nucleus (dash–dotted black). Thus the boundaries of the available  $v_{\chi,\text{Lab}}-\eta$  combinations shown in Figs. 4(b) to 4(f) shift now towards higher  $v_{\chi,\text{Lab}}$  and smaller  $\eta$  area. This implies that, as shown in Figs. 4(g) to 4(j), once the WIMP mass is  $\lesssim 45$  GeV, the angular recoil–flux distribution of the scattered xenon nuclei should be more concentrated than those with fluorine. The northern shifts would also become smaller. In Figs. 4(k) to 4(n)), while the concentration of the recoil–flux distributions

<sup>6</sup>It is basically the conventional astronomical Galactic coordinate system [12]: its coordinate axes are parallel to our Galactic coordinate system, but its origin is located at the Earth’s center. Hence, the transformation between our Equatorial and geocentric Galactic coordinate systems is a pure rotation and the relative velocity of the Earth in the Galaxy is discarded.



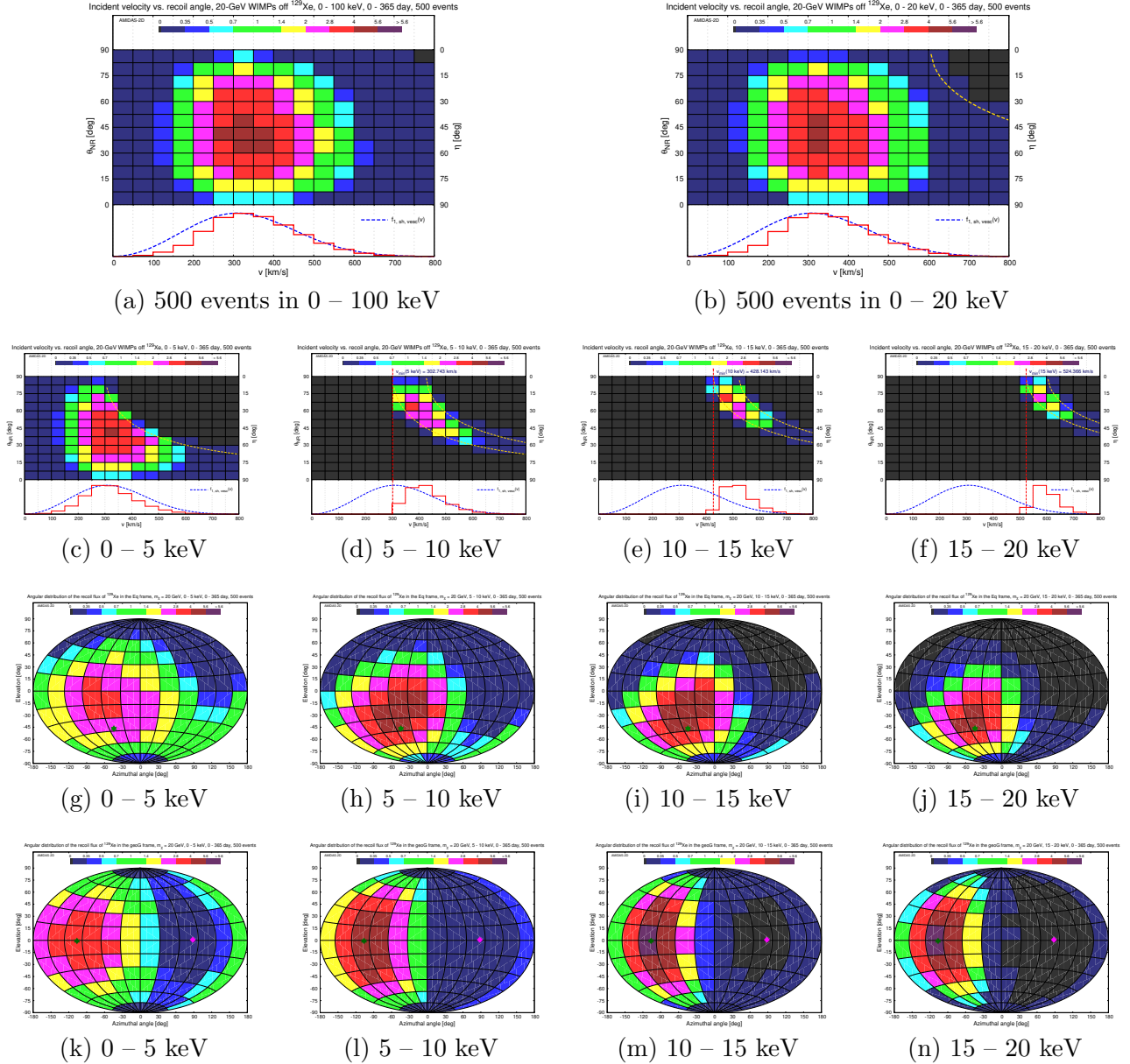
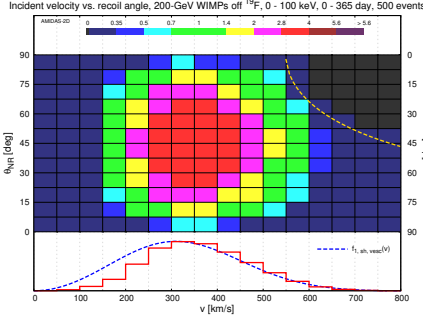


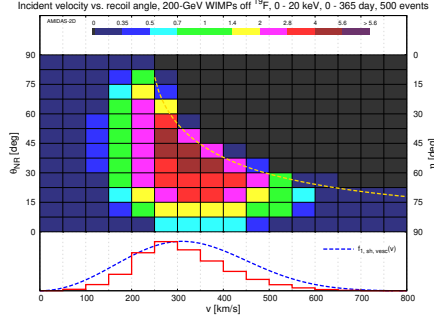
Figure 4: As Figs. 2: the mass of incident halo WIMPs is  $m_\chi = 20$  GeV, except that a heavy nucleus  $^{129}\text{Xe}$  has been considered as our target.

with the raising recoil energy window as well as the north-south-sky symmetry and the inner-outer-sky asymmetry can be observed more clearly, the decrease of the recoil fluxes on the inner and the outer skies are also sharper with the xenon nuclei than with fluorine.

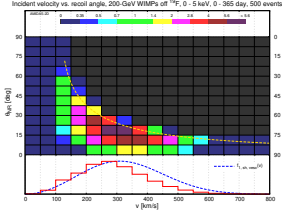
Moreover, as mentioned in Sec. 3.1, the (red) WIMP effective velocity distributions corresponding to different energy windows (especially those shown in Figs. 4(d) and 4(e)) would obviously differ from those cut simply from the (blue) compared generating velocity distribution. This would confirm clearly our theoretical prediction discussed in detail in Ref. [14] that the 1-D effective velocity distribution of the *scattering* WIMPs would not be identical to the velocity distribution of incident halo WIMPs and thus its contributions (from the same velocity range) to the differential WIMP-nucleus scattering event rates in different energy ranges could not be simply estimated by integrating over the 1-D theoretical velocity distribution (of entire halo WIMPs).



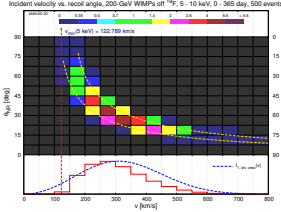
(a) 500 events in 0 – 100 keV



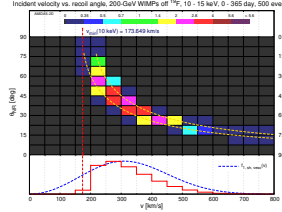
(b) 500 events in 0 – 20 keV



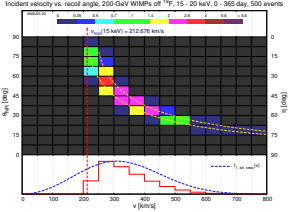
(c) 0 – 5 keV



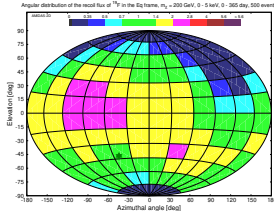
(d) 5 – 10 keV



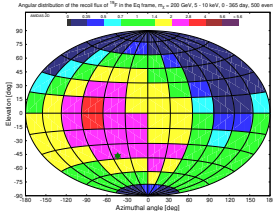
(e) 10 – 15 keV



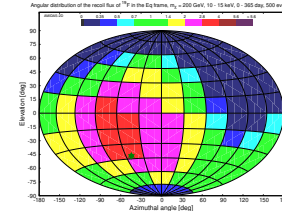
(f) 15 – 20 keV



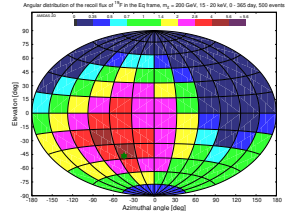
(g) 0 – 5 keV



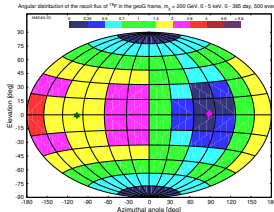
(h) 5 – 10 keV



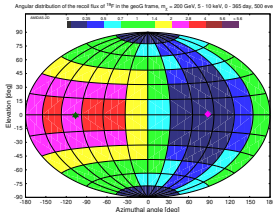
(i) 10 – 15 keV



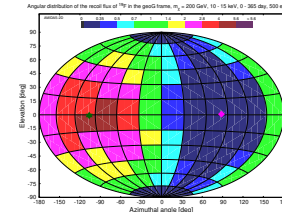
(j) 15 – 20 keV



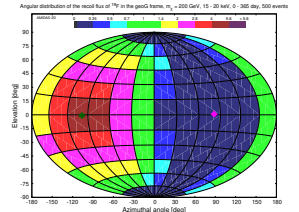
(k) 0 – 5 keV



(l) 5 – 10 keV



(m) 10 – 15 keV



(n) 15 – 20 keV

Figure 5: As Figs. 2: the light nucleus  $^{19}\text{F}$  has been considered as our target, except that the mass of incident halo WIMPs is raised to  $m_\chi = 200$  GeV.

## 4 Scattering by heavy 200-GeV WIMPs

In this section, we raise the mass of incident WIMPs to  $m_\chi = 200$  GeV.

### 4.1 200-GeV WIMPs off $^{19}\text{F}$ nuclei

As in Sec. 3.1, we consider at first the light nucleus  $^{19}\text{F}$  as our detector target.

While the difference between the  $v_{\chi,\text{Lab}}-\eta$  distributions and the (red) effective velocity distributions in Figs. 2(a) and 5(a) for the full energy range between 0 and 100 keV is pretty small, except of the four bins around  $v_{\chi,\text{Lab}} \simeq 350$  km/s and  $\eta \simeq 45^\circ$ , with a much lower upper cut-off of the analyzed energy window of 20 keV, the difference between Figs. 2(b) and 5(b) can be observed clearly. A shift of (the average velocity of) the effective velocity distribution of the

scattering WIMPs towards a lower velocity and, consequently, a shift to a *larger* most frequent recoil angle of  $\eta \simeq 52.5^\circ$  can be seen directly.

More precisely, Figs. 5(c) to 5(f) show that, with the raising WIMP mass and thus the reducing transformation constant  $\alpha$ , the most frequent recoil angle ( $\eta$ ) would be pretty large, especially in the low energy range of  $Q \leq 10$  keV. Consequently, the corresponding angular recoil–flux distributions in Figs. 5(g) to 5(j) as well as those in Figs. 5(k) to 5(n) show pretty widely spread patterns (wider than those in Figs. 2).

It should be important to notice here that, with (light target nuclei like)  $^{19}\text{F}$ , the variation of the angular recoil–flux distributions in four considered narrow energy windows shown in Figs. 5(k) to 5(n) can be seen more obviously than those induced by 20-GeV WIMPs. In addition, comparing to Figs. 2(k) to 2(n), the angular recoil–flux distribution in each corresponding energy window is now flatter. Interestingly, the inner–outer–sky asymmetry of the angular recoil–flux distribution in Fig. 5(k) show a *reverse* pattern: (the decrease of) the recoil flux on the inner (east) sky is now clearly larger (and sharper) than that on the outer (west) sky. These “WIMP–mass dependent” characteristics indicate a possibility to pin down the mass of incident halo WIMPs by using the angular recoil–energy spectra (with different target nuclei) offered by directional direct detection experiments.

## 4.2 200-GeV WIMPs off $^{129}\text{Xe}$ nuclei

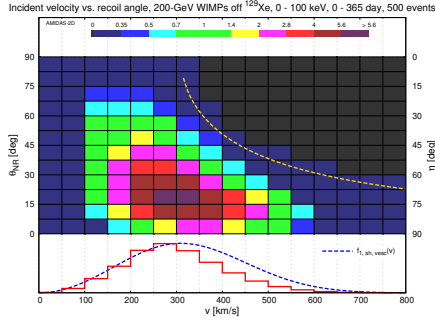
As in Sec. 3.2, we consider the heavy nucleus  $^{129}\text{Xe}$  as our detector target.

First of all, comparing Figs. 6(a) and 6(b) with Figs. 4(a) and 4(b), since  $\alpha(^{129}\text{Xe}, m_\chi = 200 \text{ GeV})$  is now pretty small ( $\simeq 0.1$ ) and the nuclear form factor suppression becomes also much stronger [11], the most frequent recoil angle would now be squeezed to only  $\eta \simeq 75^\circ$ . More precisely, in Figs. 6(c) to 6(f) for each 5-keV energy window, the most frequent recoil angle would be at least  $\eta \simeq 60^\circ$ , or even as large as  $\eta \simeq 80^\circ$ . This means that a large number of observed recoil events would be deflected almost *perpendicularly*. Hence, the angular recoil–flux distributions shown in Figs. 6(g) to 6(j) would thus be extended much wider and flatter than those in Figs. 4(g) to 4(j) (compare also the top frames of Figs. 23(a) and 23(c) of Ref. [9]).

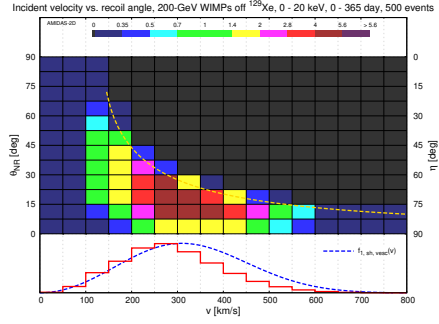
Moreover, basically due to its heavy atomic mass and in turn the reduced transformation constant  $\alpha$  as well as the strong nuclear form factor suppression and thus the large recoil angle, with (heavy target nuclei like)  $^{129}\text{Xe}$ , the difference between the angular recoil–flux distributions in four considered energy windows shown in Figs. 4 and 6 would now be strongly enlarged than those with (light target nuclei like)  $^{19}\text{F}$ . One can also find that the differences between all corresponding plots in Figs. 5 and 6 would be larger than the differences between plots in Figs. 2 and 4. Additionally, the “reverse” inner–outer–sky asymmetry of the angular recoil–flux distribution in the geocentric Galactic coordinate system observed in Fig. 5(k) could also be found here, and, perhaps due to the heavy atomic mass of xenon nuclei, even in all four considered energy windows. These indicate clearly that, comparing and/or combining the angular recoil–energy spectra with different target nuclei could provide a method for reconstructing the WIMP mass analytically (and perhaps even model–independently).

## 5 Summary

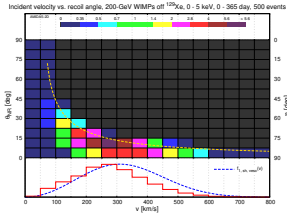
In this paper, as a supplementary of our study on the angular distribution of the recoil flux of WIMP–scattered target nuclei and on that of the WIMP effective scattering velocity distribution, we investigated the scattering probability distribution of the WIMP incident velocity versus the



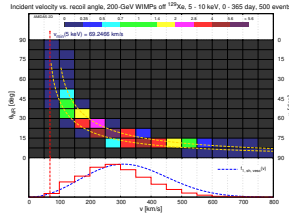
(a) 500 events in 0 – 100 keV



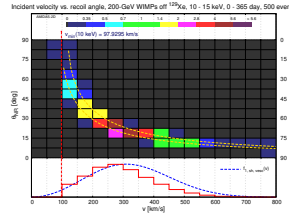
(b) 500 events in 0 – 20 keV



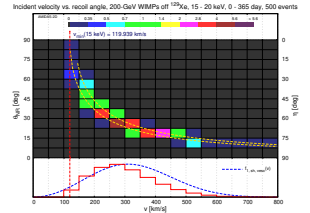
(c) 0 – 5 keV



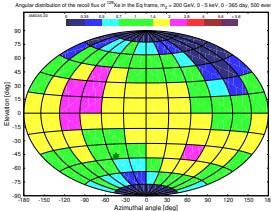
(d) 5 – 10 keV



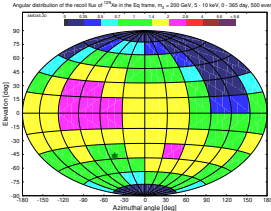
(e) 10 – 15 keV



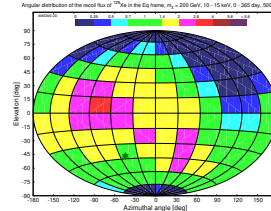
(f) 15 – 20 keV



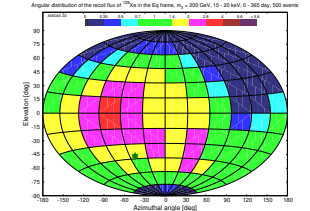
(g) 0 – 5 keV



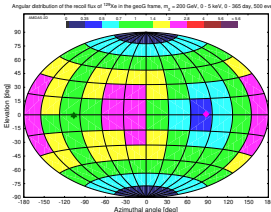
(h) 5 – 10 keV



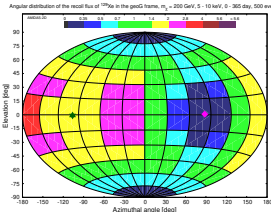
(i) 10 – 15 keV



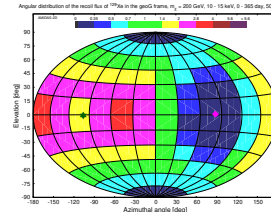
(j) 15 – 20 keV



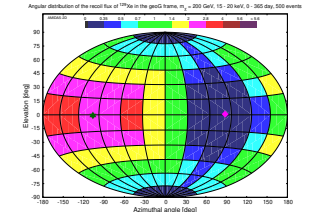
(k) 0 – 5 keV



(l) 5 – 10 keV



(m) 10 – 15 keV



(n) 15 – 20 keV

Figure 6: As Figs. 4: the heavy nucleus  $^{129}\text{Xe}$  has been considered as our target, except that the mass of incident halo WIMPs is raised to  $m_\chi = 200$  GeV.

nuclear recoil angle in narrow recoil energy windows for different WIMP masses and target nuclei.

As argued in detail in Ref. [14], our simulations show that, not only the velocity distribution of incident halo WIMPs, but also the factor of the recoil angle appearing in the differential scattering cross section could affect the scattering probability distribution of the available incident velocity–recoil angle combination constrained by the bounds of a (narrow) recoil energy window. As consequences, firstly, the scattering probability always reduces strongly (almost vanishes) around zero recoil angle ( $\eta \simeq 0$ ). Secondly, the 1-D WIMP effective velocity distributions corresponding to different narrow energy windows would not be consistent with each other nor those cut simply from the generating velocity distribution of incident halo WIMPs by the minimal–required WIMP incident velocities. And their contributions (from the same velocity range) to the differential WIMP–nucleus scattering event rates in different narrow energy win-

dows could not be the same nor simply estimated by integrating over the 1-D theoretical velocity distribution (of entire halo WIMPs).

Moreover, once the WIMP mass is as light as only a few tens GeV, for both of light and heavy target nuclei, the most recoil angles would nevertheless be small enough to maintain the angular distributions of the induced recoil events pretty concentrated (around the opposite direction of the theoretical WIMP incident direction). In contrast, once the WIMP mass is as heavy as a few hundreds GeV, the most actually-induced recoil angles (of events observed in low energy windows) could be pretty large. This means that a large number of observed recoil events would be strongly deflected (almost perpendicularly) and the corresponding angular recoil-flux distribution patterns could then be pretty wide and flat, especially when heavy nucleus like I or Xe is used as our target.

On the other hand, our simulation results demonstrated in the geocentric Galactic coordinate system show clearly the target and WIMP-mass dependence of (the variation of) the angular recoil-flux distributions in different narrow energy windows. Firstly, with the increasing WIMP mass, the angular recoil-flux distributions become flatter and the differences between the distribution patterns with different target nuclei become also larger. Secondly, while for a WIMP mass of a few tens GeV, (the decrease of) the recoil fluxes on the inner sky are clearly larger (and sharper) than those on the outer sky, once the WIMP mass is a few hundreds GeV, (the decrease of) the recoil fluxes on the outer sky could inversely be larger (and sharper) than those on the inner sky; the heavier the target nuclei, the higher the upper limit of the energy window, under which one can observe this “reverse” inner-outer-asymmetry. These indicate a possibility of (analytic and perhaps model-independent) reconstruction of the WIMP mass by comparing and/or combining the angular recoil-energy spectra with different target nuclei.

In summary, in this work we studied the elastic WIMP-nucleus scattering process and the angular recoil-energy spectrum in more details. Hopefully, this work could help our colleagues to develop methods and analyses for reconstructing properties of Galactic Dark Matter particles by using 3-dimensional information offered by directional direct detection experiments.

## Acknowledgments

This work was strongly encouraged by the “*Researchers working on e.g. exploring the Universe or landing on the Moon should not stay here but go abroad.*” speech.

## References

- [1] G. Jungman, M. Kamionkowski and K. Griest, “*Supersymmetric Dark Matter*”, *Phys. Rept.* **267**, 195–373 (1996), [arXiv:hep-ph/9506380](#).
- [2] M. Schumann, “*Direct Detection of WIMP Dark Matter: Concepts and Status*”, *J. Phys.* **G46**, 103003 (2019), [arXiv:1903.03026 \[astro-ph.CO\]](#).
- [3] L. Baudis and S. Profumo, contribution to “*The Review of Particle Physics 2020*”, *Prog. Theor. Exp. Phys.* **2020**, 083C01 (2020), *27. Dark Matter*.
- [4] J. Cooley, “*Dark Matter Direct Detection of Classical WIMPs*”, [arXiv:2110.02359 \[hep-ph\]](#) (2021).
- [5] S. Ahlen *et al.*, “*The Case for a Directional Dark Matter Detector and the Status of Current Experimental Efforts*”, *Int. J. Mod. Phys.* **A25**, 1–51 (2010), [arXiv:0911.0323 \[astro-ph.CO\]](#).

- [6] F. Mayet *et al.*, “A Review of the Discovery Reach of Directional Dark Matter Detection”, *Phys. Rept.* **627**, 1–49 (2016), [arXiv:1602.03781 \[astro-ph.CO\]](#).
- [7] S. E. Vahsen, C. A. J. O’Hare and D. Loomba, “Directional Recoil Detection”, *Ann. Rev. Nucl. Part. Sci.* **71**, 189–224 (2021), [arXiv:2102.04596 \[physics.ins-det\]](#).
- [8] C.-L. Shan, “Monte Carlo Scattering-by-Scattering Simulation of 3-Dimensional Elastic WIMP–Nucleus Scattering Events”, [arXiv:2103.06485 \[hep-ph\]](#) (2021), in publication.
- [9] C.-L. Shan, “Simulations of the Angular Recoil–Energy Distribution of WIMP–Scattered Target Nuclei for Directional Dark Matter Detection Experiments”, [arXiv:2103.06486 \[hep-ph\]](#) (2021), in publication.
- [10] C.-L. Shan, “Annual Modulations of the Angular Recoil–Flux/Energy Distributions of WIMP–Scattered Target Nuclei Observed at an Underground Laboratory”, *proceedings of the 17th International Conference on Topics in Astroparticle and Underground Physics (TAUP 2021)*, *J. Phys.: Conf. Ser.* **2156**, 012173 (2022), [arXiv:2110.05027 \[hep-ph\]](#).
- [11] C.-L. Shan, “3-Dimensional Effective Velocity Distribution of Halo Weakly Interacting Massive Particles Scattering off Nuclei in Direct Dark Matter Detectors”, [arXiv:2103.06883 \[astro-ph.HE\]](#) (2021), in publication.
- [12] C.-L. Shan, “Simulations of the 3-Dimensional Velocity Distribution of Halo Weakly Interacting Massive Particles for Directional Dark Matter Detection Experiments”, [arXiv:1905.11279 \[astro-ph.HE\]](#) (2019), in publication.
- [13] C.-L. Shan, “Simulations of the Angular Kinetic–Energy Distribution of Halo Weakly Interacting Massive Particles for Directional Dark Matter Detection Experiments”, in publication.
- [14] C.-L. Shan, “Some Thoughts on (the Incompleteness of) the (Double) Differential Event Rates for Elastic WIMP–Nucleus Scattering in (Directional) Direct Dark Matter Detection Physics”, [arXiv:2110.10920 \[hep-ph\]](#) (2021), in publication.
- [15] J. Billard, F. Mayet, J. F. Macias–Perez and D. Santos, “Directional Detection as a Strategy to Discover Galactic Dark Matter”, *Phys. Lett.* **B691**, 156–162 (2010), [arXiv:0911.4086 \[astro-ph.CO\]](#).
- [16] C. A. J. O’Hare and A. M. Green, “Directional Detection of Dark Matter Streams”, *Phys. Rev.* **D90**, 123511 (2014), [arXiv:1410.2749 \[astro-ph.CO\]](#).
- [17] C. A. J. O’Hare, B. J. Kavanagh and A. M. Green, “Time–Integrated Directional Detection of Dark Matter”, *Phys. Rev.* **D96**, 083011 (2017), [arXiv:1708.02959 \[astro-ph.CO\]](#).
- [18] C.-L. Shan, online interactive demonstrations of 3-dimensional elastic WIMP–nucleus scattering for (directional) direct Dark Matter detection experiments and phenomenology, <http://www.tir.tw/phys/hep/dm/amidas-2d/> (2021).